Chinese Journal of Chemical Engineering 68 (2024) 65–75

Contents lists available at ScienceDirect

Chinese Journal of Chemical Engineering

journal homepage: www.elsevier.com/locate/CJChE

Full Length Article

Pickering emulsion transport in skeletal muscle tissue: A dissipative particle dynamics simulation approach

Xuwei Liu [1, 2], Wei Chen [1, 4, 5, *], Yufei Xia [3, 4, 5, *], Guanghui Ma [3, 4, 5], Reiji Noda [2], Wei Ge [1, 2, 4, 5]

[1] State Key Laboratory of Mesoscience and Engineering, Institute of Process Engineering, Chinese Academy of Sciences, Beijing 100190, China
[2] Division of Environmental Engineering Science, Graduate School of Science and Technology, Gunma University, 1-5-1 Tenjin-cho, Kiryu, Gunma 376-8515, Japan
[3] State Key Laboratory of Biochemical Engineering, Institute of Process Engineering, Chinese Academy of Sciences, Beijing 100190, China
[4] School of Chemical Engineering, University of Chinese Academy of Sciences, Beijing 100049, China
[5] Innovation Academy for Green Manufacture, Chinese Academy of Sciences, Beijing 100190, China

ARTICLE INFO

Article history:
Received 7 November 2023
Received in revised form
2 January 2024
Accepted 2 January 2024
Available online 12 January 2024

Keywords:
Pickering emulsion
Skeletal muscular cells
Transport phenomena
Dissipative particle dynamics
Drug delivery

ABSTRACT

Lymph node targeting is a commonly used strategy for particulate vaccines, particularly for Pickering emulsions. However, extensive research on the internal delivery mechanisms of these emulsions, especially the complex intercellular interactions of deformable Pickering emulsions, has been surprisingly sparse. This gap in knowledge holds significant potential for enhancing vaccine efficacy. This study aims to address this by summarizing the process of lymph-node-targeting transport and introducing a dissipative particle dynamics simulation method to evaluate the dynamic processes within cell tissue. The transport of Pickering emulsions in skeletal muscle tissue is specifically investigated as a case study. Various factors impacting the transport process are explored, including local cellular tissue environmental factors and the properties of the Pickering emulsion itself. The simulation results primarily demonstrate that an increase in radial repulsive interaction between emulsion particles can decrease the transport efficiency. Additionally, larger intercellular gaps also diminish the transport efficiency of emulsion droplet particles due to the increased motion complexity within the intricate transport space compared to a single channel. This study sheds light on the nuanced interplay between engineered and biological systems influencing the transport dynamics of Pickering emulsions. Such insights hold valuable potential for optimizing transport processes in practical biomedical applications such as drug delivery. Importantly, the desired transport efficiency varies depending on the specific application. For instance, while a more rapid transport might be crucial for lymph-node-targeted drug delivery, certain applications requiring a slower release of active components could benefit from the reduced transport efficiency observed with increased particle repulsion or larger intercellular gaps.

1. Introduction

Pickering emulsions, a century-old discovery, have witnessed a resurgence in interest in recent decades. Their unique stabilization mechanism, facilitated by solid particles at the oil–water interface, sets them apart from traditional emulsions. By leveraging solid particles as stabilizers instead of conventional surfactants, Pickering emulsions exhibit enhanced stability against coalescence and present a myriad of advantageous properties. When designed with biocompatible solid particles, these emulsions become particularly promising for *in vivo* applications, leading to widespread adoption in diverse sectors ranging from biomedicine to cosmetics [1]. Xia *et al.* [2] harnessed the immunogenic properties of Pickering emulsions for use as vaccine adjuvant and delivery strategy. This highlighted the distinct softness and flexibility of Pickering emulsion in cellular interactions, showing its vast promise for biomedical uses. Present investigations predominantly focus on the stability mechanisms, biocompatibility, factors affecting the delivery process [3–6], and some potential applications in parenteral and mucosal drug delivery, vaccines, and cell-based therapies [7]. Presently, scholar investigations into Pickering emulsions for drug delivery predominantly focus on a macroscopic and rather cursory

* Corresponding authors.
E-mail addresses: chenwei@ipe.ac.cn (W. Chen), yfxia@ipe.ac.cn (Y. Xia).

https://doi.org/10.1016/j.cjche.2024.01.002
1004-9541/

general analysis. Comprehensive studies elucidating the intracorporeal delivery mechanisms of Pickering emulsions, particularly the intricate intercellular interactions of deformable Pickering emulsions, remain conspicuously scant and have historically garnered minimal attention but a pivotal role in vaccine efficacy.

Lymph nodes (LNs) play a pivotal role in the immune system, acting as hubs to collect immunological data from surrounding tissues. Packed with a variety of lymphocytes such as antigen-presenting cells (APCs), B cells, and T cells, LNs are crucial centers for initiating adaptive immune reactions and facilitating efficient antigen presentation, cellular interactions, and expansion. Consequently, vaccines targeting the LNs hold significant promise for directly interacting with APCs, triggering potent antibody secretion, T-cell responses, and anti-tumor effects [8,9]. For particulate vaccines, such as Pickering emulsions, they can carry antigens into the LNs, enhancing the immune response through interactions with immune cells. In addition, LN targeting is a commonly used strategy in particulate vaccines [10–12]. However, the quantitative analysis and simulated model are still limited, especially for the soft and deformable droplets such as Pickering emulsions.

There remains a limited depth of understanding and simulation of the internal kinematics within tissues within the human body for this topic. Therefore, in order to elucidate the delivery process of Pickering emulsion within the human body more comprehensively, according to some research works for the physiological structure related to the transport of vaccines [2,13–21], this study summarizes the typical process of LN-targeting transport, which encompasses a series of steps: intramuscular injection, intercellular transport in skeletal muscular tissue, entry into the initial lymphatic capillaries, transport through lymphatic vessels, and finally, accumulation in the LNs. The SEM images [13,15,22] show the physiological relationship and structure of related tissues and cells; Furthermore, we schematically illustrate the LN transfer process of soft droplets in Fig. 1. Muscle cells, also known as muscle fibers, are observed within muscle tissues, specifically in skeletal muscles here. Morphologically, these cells are elongated and are tubular in shape. Muscle fibers are essentially muscle cells and serve as the fundamental units of muscles. Each muscle fiber is composed of numerous myofibrils. Typically, the length of a muscle fiber ranges from a few millimeters to several centimeters (2–3 cm), with a diameter spanning approximately from 10 to 100 μm [15,18]. Lymphatic endothelial cells (LECs), which are 14–66 μm in length [13] and 50–100 nm in thickness [17], form specialized cell-to-cell junctions. Capillary lymphatics absorb lymph fluid through open "button-like" junctions between LECs, the about-3-to-4-μm-wide [13] and loosely overlapping pillows of which are exposed to interstitial to intraluminal pressure gradients to open and to close [14,22,23], while collecting vessels transport the lymph fluid to the LN through tight "zipper-like" junctions to prevent lymph leakage [13,21]. For the Pickering emulsion, the diameter of the emulsion droplets ranges between 330 nm and 500 nm, with the larger droplets measuring approximately 1.6 μm [2,7,9].

Despite the potential of deformable Pickering emulsions in vaccine delivery, both experimental and simulated studies on this topic remain sparse. In terms of experiments, with the size of the cell gap ranging from 20 to 100 nm, it is difficult for solid particles to pass through the cellular gaps and concentrate within the LNs [24]. As an alternative strategy, Song *et al.* [9] explored the deformability of an albumin-stabilized Pickering emulsion. Though, the size of the emulsion droplet (~330 nm) was larger than three times the intercellular gap, the cell-mimic deformability granted the droplets to attach and squeeze themselves between the cell gaps under the interstitial flow and adjust the droplet size to cross the endothelial cell gap. This allows the deformable Pickering emulsion to achieve high LN retention of the vaccines and induces increased immune activations. Therefore, the quantitative analysis and mathematic models are expected to elucidate the process details and offer implications to optimize novel Pickering emulsions with higher LN transport efficiency and immunogenicity. In terms of simulation, no direct relevant research has been found yet, till now. Recent advances, such as the simulation work [25] and other related work [26–28], have showcased the potential of multiscale modeling and dissipative particle dynamics (DPD) in understanding the behavior of biological systems and inspire the simulation of this research.

Given the limited research on the deformability of Pickering emulsions and the transport of vaccines in the human body, this research seeks to delve into the microscopic perspective of the deformability of Pickering emulsions as they traverse this intricate transport pathway. By doing so, we aim to provide targeted design strategies for flexible particle vaccine design, enhancing vaccine transport efficiency and the subsequent immune response. From the previous analyses of targeting LN transfer, we could find the possibilities of fluid pathway due to the physiological function and anatomical structures of lymph capillaries, besides the cellular pathway [20]. In this research, we first investigate the transport process in the skeletal muscular tissues; Furthermore, we integrate and produce a framework for three-dimensional (3D) cell modeling and dynamics analysis in cellular tissues beyond blood-flow simulation.

2. Abstraction

2.1. Model simplification

In the consideration of simplifying the model, a uniform layer of cells is modeled to represent the process of flexible particles traversing the tissue layer of muscular cells. Each cell is modeled as a capsule-like structure, which resembles the shape of muscle cells. The cells are uniformly sized and evenly distributed, with consistent intercellular gaps. The upper part of the cell layer is represented as the interior of the part of the muscle tissues. The flexible particles cross the cell gap from the upper part of the cell layer to the lower part of the cell layer, and this process is used to represent the process of the flexible particles crossing the part of the fascicle in the muscle tissue, thus allowing the Pickering emulsion to better carry out the next process to transport into the capillary of the immune system. The liquid filling the simulation box is modeled implicitly. To simplify the model and streamline the computational process, this study does not consider the adhesion between cells.

The entire simulation box is divided into the following order from top to bottom according to the actual physical model: boundary—free-motion zone—fixed-cell zone—free-motion zone—boundary. The middle layer of the simulation box is set as a cell layer to represent the position of the intercellular matrix binding to the muscle cells by fixing the position of certain points on the cells, while the cells, as a whole, can maintain a certain viscoelasticity to show the morphological changes of the cells when the flexible particles cross the cell gap. The two sides of the simulated box immediately adjacent to the fixed-cell zone are the free-motion zones, where the flexible particles move freely imposing additional constraints and additional forces. In the top free-motion zone, new particles can be added at certain initial velocities, so that the flexible particles exhibit a top-to-bottom direction of motion. A layer of fixed DPD particles is set at the top and bottom of the box to indicate the boundary, which restricts the motion of the flexible particles to prevent them from crossing the boundary of the simulated box. The illustration is shown in Fig. 2.

Based on the morphological and mechanical properties analysis of cells and Pickering emulsions, the diameter of muscle cells is approximately 20 μm [15], with a Young's modulus of about 12 kPa

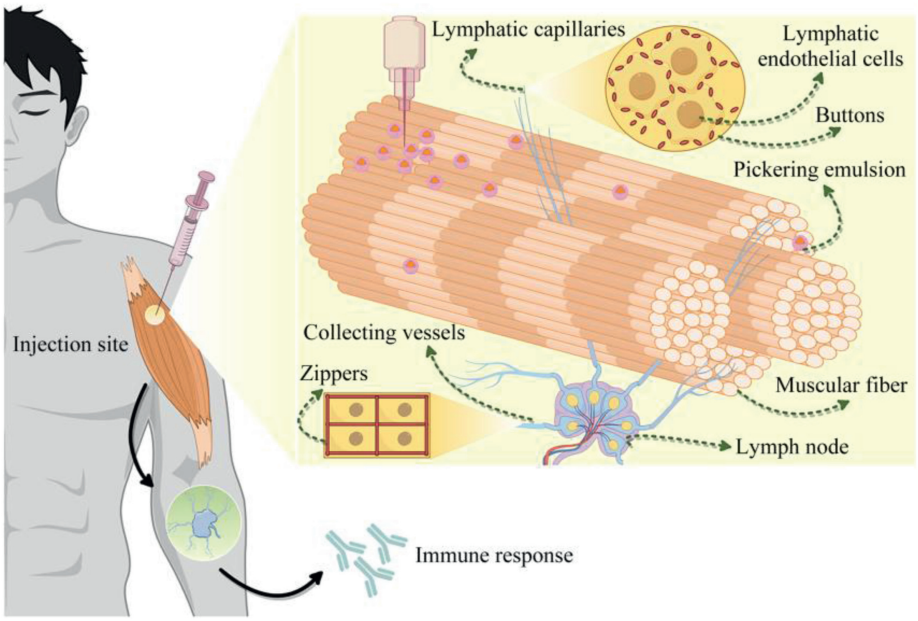

Fig. 1. Schematic illustration on the lymph node transfer of soft droplets.

[29]. The Pickering emulsion has a diameter of around 500 nm and a Young's modulus of approximately 36.5 MPa [9]. In this context, the Pickering emulsion can be considered as a rigid particle. Drawing on the triangular lattice spring network derived from hemoglobin modeling, and rationalizing the process of flexible particles traversing the cell gap, a capsule-type layer of cells lined up side by side as the part of muscular tissue was constructed separately, and DPD particles were constructed to represent the Pickering emulsion, and different viscoelastic parameters were set to reflect the different viscoelasticity between the cells and the particles. The cells are evenly distributed with the beads on the surface. Two adjacent beads will form an adhesive element, three adjacent beads will form a triangular element, and two triangular elements that share an edge will form a bending element.

2.2. Extraction of physical quantities

To characterize the physical system of the model, it is necessary to first confirm the physical quantities in the real world, which are summarized in Table 1. L_0^{P} represents the characteristic length, where the diameter of muscle fibers is adopted as the characteristic length in this context, typically falling within the range of 10–100 μm [15]. The value of $(k_{\mathrm{B}}T)^{\mathrm{P}}$ is taken at the temperature $T = 296$ K. $N_{\mathrm{v}}^{\mathrm{P}}$ and $N_{\mathrm{s}}^{\mathrm{P}}$ represent the number of actins and spectrins in biology, respectively, but in the modeling process, a rough estimate was made as the impact of different levels of coarse-graining on the mechanical properties and deformability of the cell is not pronounced [30]. Based on the finite element analysis, the result $Y^{\mathrm{P}} = 3\mu_0^{\mathrm{P}}$ was obtained, which aligns well with the experimental observations [25]. Here, the 'P' in the superscript stands for physical units.

3. Mathematical Framework

3.1. DPD simulation method

DPD is a coarse-grained molecular dynamics model, in which a particle represents a cluster of many molecules, and the interactions consist of conserved, dissipative, and stochastic forces [31,32]. As a coarse-grained molecular dynamics (CGMD) model, DPD follows the coarse-grained procedure described earlier. Newton's second law describes the controlling equation for each particle. Thus the equation of motion of the particles can be described as follows:

$$\frac{\mathrm{d}\boldsymbol{r}_i}{\mathrm{d}t} = \boldsymbol{v}_i \tag{1}$$

$$m_i \frac{\mathrm{d}\boldsymbol{v}_i}{\mathrm{d}t} = \sum_{i \neq i'} \left(\boldsymbol{f}_{ii'}^{\mathrm{DPD}} + \boldsymbol{f}_{\mathrm{e}} \right) \tag{2}$$

m_i is the mass of particle i, which is generally set to 1 to simplify the calculation. $\boldsymbol{f}_{\mathrm{e}}$ is the additional extra force, which is exerted on the particle. The force $\boldsymbol{f}_{ii'}^{\mathrm{DPD}}$ consists of three parts: conservative force $\boldsymbol{f}_{ii'}^{\mathrm{C}}$, dissipative force $\boldsymbol{f}_{ii'}^{\mathrm{D}}$ and random force $\boldsymbol{f}_{ii'}^{\mathrm{R}}$.

The conservative force is

$$\boldsymbol{f}_{ii'}^{\mathrm{C}} = a_{ii'} w^{\mathrm{C}}(r_{ii'}) \tag{3}$$

The dissipative force is

$$\boldsymbol{f}_{ii'}^{\mathrm{D}} = \sum_{i \neq i'} -\gamma_{ii'} w^{\mathrm{D}}(r_{ii'}) (\boldsymbol{e}_{ii'} \cdot \boldsymbol{v}_{ii'}) \boldsymbol{e}_{ii'} \tag{4}$$

The random force is

$$\boldsymbol{f}_{ii'}^{\mathrm{R}} = \sum_{i \neq i'} \sigma_{ii'} w^{\mathrm{R}}(r_{ii'}) \theta_{ii'} \boldsymbol{e}_{ii'} = \sum_{i \neq i'} \sigma_{ii'} w^{\mathrm{R}}(r_{ii'}) \zeta_{ii'} \Delta t^{-\frac{1}{2}} \boldsymbol{e}_{ii'} \tag{5}$$

The conservative force acts as a soft potential along the center-to-center distance between particles, representing the chemical properties of the DPD system. It is derived from pairwise interaction potentials between neighboring particles, where $a_{ii'}$ is the repulsive force parameter that determines the strength of their collisions. $w^{\mathrm{C}}(r_{ii'})$ is the conservative force mass function, which is generally the standard weight function $w^{\mathrm{C}}(r_{ii'}) = 1 - \frac{r_{ii'}}{r_c}$, where $r_{ii'}$ is the interparticle distance, $\boldsymbol{r}_{ii'} = \boldsymbol{r}_i - \boldsymbol{r}_{i'}$, $r_{ii'} = |\boldsymbol{r}_{ii'}|$, and

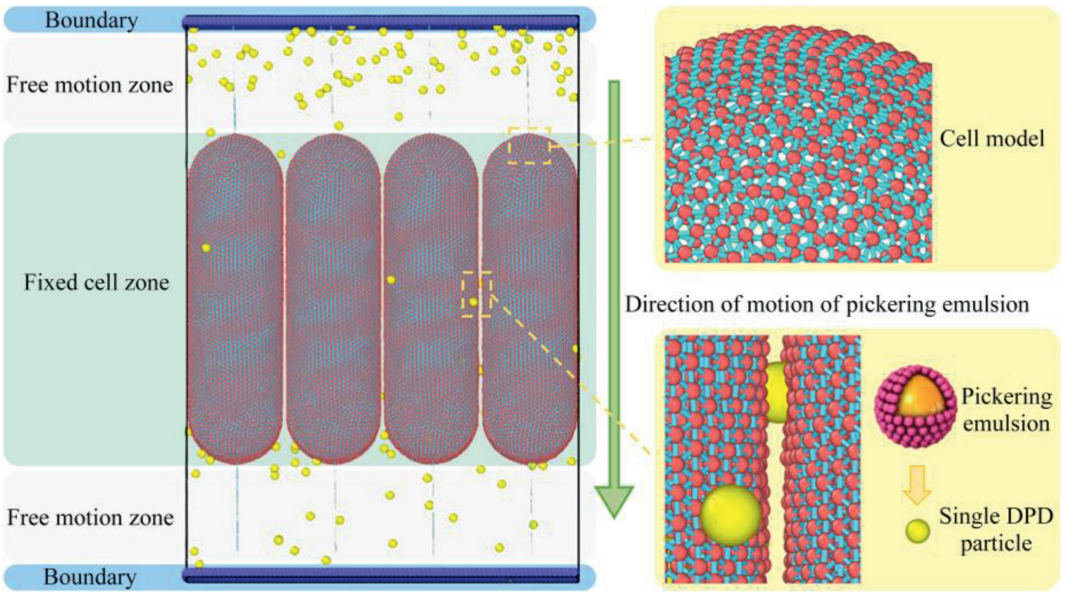

Fig. 2. Illustration of the simplified model.

r_c is the truncation radius, which indicates the effective range of force exerted between particles and is usually considered as the unit length, *i.e.*, $r_c = 1$. $\boldsymbol{e}_{ii'}$ denotes the unit vector between particle i and particle j, taken as $\boldsymbol{e}_{ii'} = \frac{\boldsymbol{r}_{ii'}}{r_{ii'}}$, with the direction from i' to i.

The random force mass function $w^R(r_{ii'})$ is to be chosen as the equation $w^R(r_{ii'}) = \left[1 - \left(\frac{r_{ii'}}{r_c}\right)\right]^{m^R}$. In the standard DPD method, the parameter m^R was initially fixed at 1. However, varying the exponent values allows for the adjustment of fluid viscosity, consequently leading to an increase in the Schmidt number [33,34].

According to the fluctuation-dissipation theorem [35], temperature regulation is realized by striking a balance between random and dissipative force, and we can obtain the relationship of the dissipative force mass function $w^D(r_{ii'})$ and $w^R(r_{ii'})$, dissipative forces coefficient $\gamma_{ii'}$, and random forces coefficient $\sigma_{ii'}$:

$$w^D(r) = \left[w^R(r_{ii'})\right]^2, \sigma_{ii'}^2 = 2\gamma_{ii'}k_BT \tag{6}$$

where T is the temperature and k_B is the Boltzmann constant.

In excess of the cutoff r_c, the interparticle force of particles vanishes to zero. According to the view of fluid particle model [36] and single dissipative-particle-dynamics particles model [27,37,38], we could consider a DPD particle to represent one real particle in the simulation.

3.2. Mesoscale viscoelastic membrane model

3.2.1. Introduction of mesoscale viscoelastic membrane model

The mesoscale viscoelastic membrane model (MVMM) has evolved from the development of mesoscale models for red blood cells. The cell membrane of red blood cells consists of a lipid bilayer supported by an internal cytoskeleton. The cytoskeleton, composed of a compact network of spectrins and actins, provides structural stability. The viscosity, elasticity, and bending stiffness of the membrane are derived from the physical properties of these biological components. The development history of this model is summarized as follows: first, a spring-based network model was introduced and was subsequently refined as a discrete representation of hemoglobin at the protein level [39,40]; Secondly, building on this foundation, a systematic coarse-graining method was crafted, considerably reducing the number of degrees of freedom [30]; Thirdly, this simplified model was further optimized to deliver accurate mechanical responses [25]; Fourth, this spring-based network model has more applications in some similar fields, such as the deformation and marginalization of white blood cells [41], modelling rigid nanoparticles in the simulation of their evolution in endocytosis within the cell membrane [26], even the simulation of complete blood flow [42]. In addition, the mesoscale viscoelastic membrane model is constantly evolving not only in combination with standard DPD methods but also extending to CGMD [43], lattice Boltzmann method [44], and transport DPD [45] mesoscale numerical simulation methods.

3.2.2. Numerical model

The cell membrane model consists of a set of vertices (DPD particles) and the two-dimensional (2D) triangular network they form, with the N_v vertices interconnected to form N_s edges and subsequently N_t triangles. The total energy describing the triangular network model could be divided into four different parts, such as in-plane elastic viscous dissipative energy, bending energy, surface area energy, and volume energy, which are labeled by U_{IP}, U_B, U_A, and U_V, respectively [46].

$$U(\{\boldsymbol{r}_i\}) = U_{IP} + U_B + U_A + U_V \tag{7}$$

The in-plane energy is given by the following equation:

$$U_{IP} = \sum_{j=1}^{N_s}\left[U_{IPS}(l_j) + U_{IPV}(\Delta v_j)\right] + \sum_{k=1}^{N_t}\frac{C_q}{A_k^q} \tag{8}$$

In the equation, IPS and IPV represent the in-plane spring energy and the in-plane viscous dissipation, respectively. The first summation term in the equation expresses the contribution of the viscous springs; l_j is the length of the j-th spring, and Δv_j is the difference in relative velocities at the ends of the spring. The second term represents the summation of the elastic energy stored in each triangular piece of network segment from the physical viewpoint, where A_k is the area of the k-th triangle.

Table 1
Physical quantities in physical units

Physical quantity		Value	
Symbol	Meaning	Cell	Droplet
L_0^{P}	Characteristic length	20×10^{-6} m	0.5×10^{-6} m
$(k_{\mathrm{B}}T)^{\mathrm{P}}$	Energy unit per unit particle mass	1.0867×10^{-21} J	4.0867×10^{-21} J
$N_{\mathrm{v}}^{\mathrm{P}}$	Number of vertices	–	–
$N_{\mathrm{s}}^{\mathrm{P}}$	Number of springs	–	–
μ_0^{P}	Linear shear modulus	6.3×10^{-6} J·m^{-2}	–
Y^{P}	Young's modulus	18.9×10^{-6} J·m^{-2}	–
η^{P}	Viscosity	0.022 Pa·s	0.0013 Pa·s
$k_{\mathrm{c}}^{\mathrm{P}}$	Bending rigidity	2.4×10^{-19} J	–

A more concise and intuitive model consisting of the potential energy of the worm-like chain (WLC) model and power function (POW) is adopted here, as shown in the following equation:

$$U_{\mathrm{IP}} = \sum_{j=1}^{N_s} U_{\mathrm{WLC}} + \sum_{j=1}^{N_s} U_{\mathrm{POW}} = \sum_{j=1}^{N_s} \left[\frac{k_{\mathrm{B}}Tl_{\mathrm{m}}\left(3x_j^2 - 2x_j^3\right)}{4p(1-x_j)} + \frac{k_{\mathrm{p}}}{(m-1)l_j^{m-1}} \right] \tag{9}$$

where $x_j = \frac{l_j}{l_{\max}} \in (0,1)$, where $l_{\max}$, p, k_{p}, and m represent the maximum spring extension, the persistence length, the spring constant, and the specified exponent, respectively. The attractive forces exerted by the WLC springs cause the components to contract. The force produced by POW model can neutralize the contractility of the triangular surface bases. The combined action of both can generate an equilibrium spring length and, in this way, p and k_{p} can be obtained from the relationship of the related parameters from the WLC model and the selected exponent n. At this point, the stored elastic energy can be ignored and C_{q} can be set to 0 [46].

The bending energy is concentrated on the edges of the two adjacent neighbor triangular segments from each other to maintain cell shape and resist bending deformation, and the bending potential energy is shown as follows:

$$U_{\mathrm{B}} = \sum_{j=1}^{N_s} k_{\mathrm{b}}\left[1 - \cos(\varphi_j - \varphi_0)\right] \tag{10}$$

where k_{b}, φ_j, and φ_0 are the bending modulus, the instantaneous angle between two adjacent triangles sharing a common edge j, and the spontaneous angle, respectively.

In Eq. (7), the last two terms represent the conservation of the cell membrane area and the incompressibility of the internal fluid, respectively, by enforcing area and volume constraints to maintain the cell shape.

$$U_A = \frac{k_{\mathrm{a}}}{2A_0^{\mathrm{tot}}}\left(A - A_0^{\mathrm{tot}}\right)^2 + \frac{k_{\mathrm{d}}}{2A_0}\sum_{k=1}^{N_t}(A_k - A_0)^2 \tag{11}$$

$$U_V = \frac{k_{\mathrm{v}}}{2V_0^{\mathrm{tot}}}(V - V_0^{\mathrm{tot}})^2 \tag{12}$$

where, k_{a}, k_{d}, k_{v}, A, V, A_0^{tot}, and V_0^{tot} are the constraint coefficients of the global area, constraint coefficients of the local area, constraint coefficients of volume, the instantaneous total area, total volume, the specified total area, and total volume, respectively.

The forces $\boldsymbol{f}_i^{\mathrm{MVMM}}$ on the nodes can be obtained by taking the derivative of the elastic network energy:

$$\boldsymbol{f}_i^{\mathrm{MVMM}} = -\frac{\partial U(\{\boldsymbol{r}_i\})}{\partial \boldsymbol{r}_i} \tag{13}$$

3.2.3. Membrane mechanical properties

According to the analysis for a node in a segment of a 2D hexagonal network of equilateral triangles and the virial theorem [47–50], the Cauchy stress at node $\boldsymbol{v}$ is obtained by the following equation:

$$\tau_{\alpha\beta} = -\frac{1}{S}\left[\frac{f(r_1)}{r_1}r_1^{\alpha}r_1^{\beta} + \frac{f(r_2)}{r_2}r_2^{\alpha}r_2^{\beta} + \frac{f(|\boldsymbol{r}_2 - \boldsymbol{r}_1|)}{|\boldsymbol{r}_2 - \boldsymbol{r}_1|}\left(r_2^{\alpha} - r_1^{\alpha}\right)\left(r_2^{\beta} - r_1^{\beta}\right)\right] - \left(q\frac{C_q}{A_k^{q+1}} + \frac{k_{\mathrm{a}}\left(A_0^{\mathrm{tot}} - N_tA\right)}{A_0^{\mathrm{tot}}} + \frac{k_{\mathrm{d}}(A_0 - A)}{A_0}\right)\delta_{\alpha\beta} \tag{14}$$

where α and β represent x or y; $f(r)$, N_t, $\delta_{\alpha\beta}$, and S are the spring force, the total number of triangles, the Kronecker delta, and the area of the hexagonal element centered at $\boldsymbol{v}$, respectively. $A_0^{\mathrm{tot}} = N_tA_0$.

Shear modulus. The shear modulus can be represented as $\mu_0 = \partial\tau_{xy}/\partial y\big|_{\gamma=0}$, which can be obtained by taking the derivative of the stress tensor with respect to the applied shear strain γ.

$$\mu_0 = \frac{\sqrt{3}k_{\mathrm{B}}T}{4pl_{\mathrm{m}}x_0}\left(\frac{x_0}{2(1-x_0)^3} - \frac{1}{4(1-x_0)^2} + \frac{1}{4}\right) + \frac{\sqrt{3}k_{\mathrm{p}}(m+1)}{4l_n^{m+1}} \tag{15}$$

Compression modulus. The linear elastic area compression modulus K is concluded from the calculation of the in-plane pressure by the minus area expansion, and the pressure is given by the following equation:

$$p = -\frac{1}{2}(\tau_{xx} + \tau_{yy}) = \frac{3l}{4A}f(l) + q\frac{C_{\mathrm{q}}}{A_k^{q+1}} + \frac{(k_{\mathrm{a}} + k_{\mathrm{d}})(A_0 - A)}{A_0} \tag{16}$$

The compression modulus K is then defined as follows:

$$K = -\frac{\partial P}{\partial \lg(A)}\Big|_{A=A_0} = -\frac{1}{2}\frac{\partial P}{\partial \lg(l)}\Big|_{l=l_0} = -\frac{1}{2}\frac{\partial P}{\partial \lg(x)}\Big|_{x=x_0} \tag{17}$$

$$K=\frac{\sqrt{3}k_BT}{4pl_m(1-x_0)^2}\left[\left(q+\frac{1}{2}\right)\left(4x_0^2-9x_0+6\right)+\frac{1+2(1-x_0)^3}{1-x_0}\right]+k_a+k_d \tag{18}$$

$$K=2\mu_0+k_a+k_d \tag{19}$$

Furthermore, we can obtain the Young's modulus and Poisson's ratio as follows:

$$Y=\frac{4K\mu_0}{K+\mu_0}, Y\to 4\mu_0, \text{if } K\to\infty \tag{20}$$

$$\nu=\frac{K-\mu_0}{K+\mu_0}, \upsilon\to 1, \text{if } K\to\infty \tag{21}$$

In practice, we use values of $\mu_0 = 100$ and $k_a + k_d = 5000$, which produce a Young's modulus of the approximately incompressible membrane, about 2% less than its asymptotic value of $4\mu_0$ [46].

Bending rigidity. The connection between the bending modulus k_b and the macroscopic membrane-bending stiffness k_c can be deduced from a hypothesis of spherical shell. By equating the macroscopic bending energy and E_B, and deriving the spontaneous angle φ_0 based on the number of the whole nodes N_v on the spherical surface, we obtain the following equation:

$$k_b=\frac{2}{\sqrt{3}}k_c, \theta_0=\cos^{-1}\left(\frac{\sqrt{3}(N_v-2)-5\pi}{\sqrt{3}(N_v-2)-3\pi}\right) \tag{22}$$

Membrane viscosity. For the membrane viscosity aspect of the mesoscale viscoelastic membrane model, the influence of original DPD dissipative force and random force is insufficient. Referring to the fluid particle model [36], the dissipative force term in standard DPD is modified as follows [46]:

$$\boldsymbol{f}_{ij}^{D}=-\gamma^{T}\boldsymbol{v}_{ij}-\gamma^{C}(\boldsymbol{v}_{ij}\cdot\boldsymbol{e}_{ij})\boldsymbol{e}_{ij} \tag{23}$$

The first term in the equation provides the dominant viscous contribution, whereas the second term is similar with the dissipative force of standard DPD. γ^T and γ^C are dissipative coefficients. According the general fluid particle model and the fluctuation–dissipation relationship, the random force is adjusted accordingly, and the details of calculation could be found in software [45,51]. The shear stress τ_{xy} over a brief period can be estimated, based on the contribution of the dissipative force in the aforementioned equation.

$$\tau_{xy}=\dot{\gamma}\left(\gamma^{T}+\frac{1}{4}\gamma^{C}\right) \tag{24}$$

where $\dot{\gamma}$ is the constant shear rate. Hence, the membrane viscosity is given by the following equation:

$$\eta_m=\frac{\tau_{xy}}{\dot{\gamma}}=\sqrt{3}\left(\gamma^{T}+\frac{1}{4}\gamma^{C}\right) \tag{25}$$

This equation indicates that γ^T constitutes the major part of membrane dissipation. Consequently, the numerical outcomes exhibit minimal sensitivity to the value of γ^C. Given the elevated values of γ^C might induce numerical instability in the simulations, it is often set to the minimum value of $\frac{\gamma^T}{3}$ [46].

3.3. Physical quantities in model units and parameters of the model

In the context of a mathematical-framework-based model, the physical quantities and model parameters, represented in model units, are summarized in Tables 2 and 3. Model units and scaling factors will be discussed in the next section. Since the Young's modulus (3D) Y_V^P of the emulsion droplet is much larger than that of the cell, and the volume of the emulsion droplet is much smaller than that of the cell, the emulsion droplet can be regarded as a rigid sphere passing through the cell gap, and the deformability is mainly reflected in the flexibility of the cell. Therefore, the mesoscale viscoelastic membrane model is still used to represent the cell, and the DPD particle is used to represent the emulsion droplet, and the cut-off radius of DPD force on the DPD particle is set to control the volume of emulsion droplet.

L_0^M, N_c^M, N_s^M, A_0^{tot}, and V_0^{tot} presented are extracted from the establishment to the model. l_0 and A_0 are mean values obtained from mesh-generation statistical results due to the stress-free model. According to Eqs. (9) and (15), k_p and p could be obtained by the μ_0^M equation and equating by attractive- and repulsive-force formula and be auto-calculated in the software without the need of input [25,51]. σ^C and σ^T are auto-calculated in the software according to the Eq. (6) and $(k_BT)^M$. k_c^M is calculated by k_c^P and energy unit ξ. In the simulations, μ_0^M, k_a, k_d, k_v, γ^T, and γ reference to other works [42,46].

4. Details of Simulation

4.1. Unit-scaling analysis

In the development of a coarse-grained cellular model, the physical quantalities and parameters of DPD model in the model must be scaled with physical units. The length scale factor λ is based on the characteristic length at equilibrium, L_0^M, where $[L_0^M]=\lambda$ and the M represents model units. λ (m) can be obtained by the following formula:

$$\lambda=\frac{L_0^P}{L_0^M} \tag{26}$$

The Young's modulus (2D) is utilized for an additional input parameter for energy scaling process. An energy-scaling factor ξ (J) is obtained by dimensional analysis of Young's modulus Y:

$$\xi=(k_BT)^M=\frac{Y^P}{Y^M}\left(\frac{L_0^P}{L_0^M}\right)^2=\frac{Y^P}{Y^M}\left(\frac{L_0^P}{L_0^M}\right)^2(k_BT)^P \tag{27}$$

where k_BT represents a unit of energy from Boltzmann's constant and temperature in the field of thermodynamics and statistical mechanics. Furthermore, force-scaling factor ε (N) and pressure-scaling factor ν (Pa) can be obtained by the following equation:

$$\varepsilon=\frac{Y^P}{Y^M}\frac{L_0^P}{L_0^M}=\frac{\xi}{\lambda} \tag{28}$$

$$\nu=\frac{\xi}{\lambda^3} \tag{29}$$

Based on dimensional analyses of viscosity η and Newton's second law, time-scaling factor τ (s) and mass-scaling factor μ (kg) can be calculated as follows:

Table 2
Physical quantities in model units

Physical quantity			Value	
Symbol	Meaning	Notice	Cell	Droplet
L_0^{M}	Characteristic length		20λ	0.5λ
$(k_{\mathrm{B}}T)^{\mathrm{M}}$	Energy unit per unit particle mass		0.0848596ξ	0.0848596ξ
$N_{\mathrm{c}}^{\mathrm{M}}$	Number of vertices		5206	–
$N_{\mathrm{s}}^{\mathrm{M}}$	Number of springs		15612	–
μ_0^{M}	Linear shear modulus	set	$100\xi/\lambda^2$	–
K^{M}	Linear-elastic area-compression modulus	By Eq. (19)	$5200\xi/\lambda^2$	–
Y^{M}	Young's modulus	By Eq. (20)	$392.453\xi/\lambda^2$	–
ν^{M}	Poisson's radio	By Eq. (21)	0.962	–
η^{M}	Viscosity	By Eq. (25)	$168.87\nu\cdot\tau$	–
$k_{\mathrm{c}}^{\mathrm{M}}$	Bending rigidity		5.016502564ξ	–

Table 3
Parameters of the model

Parameters of Models			Value	
Symbol	Meaning	Notice	Cell	Droplet
r_{c}	Cut-off distance for DPD particle		1.58λ	0.5λ
l_0	Equilibrium length	In Eq. (9)	8.581768λ	–
x_0	Maximum spring extension ratio	In Eq. (9)	2.2	–
l_{m}	Maximum spring extension	In Eq. (9), $l_{\mathrm{m}} = x_0 l_0$	18.87988λ	–
p	Persistence length	In Eq. (9)	–	–
k_{p}	POW force coefficient	In Eq. (9)	–	–
m	Exponent in POW function	In Eq. (9)	2.0	–
k_{a}	Global area constraint constants	In Eq. (11)	$4900\xi/\lambda^2$	–
k_{d}	Local area constraint constants	In Eq. (11)	$100\xi/\lambda^2$	–
k_{v}	Volume constraint constants	In Eq. (12)	$5000\xi/\lambda^2$	–
A_0^{tot}	Desired total area	In Eq. (11)	$627623.11\lambda^2$	–
A_0	Desired local area	In Eq. (11)	$31.794484\lambda^2$	–
V_0^{tot}	Desired total volume	In Eq. (12)	$15414172.6\lambda^3$	–
a	DPD conservative force coefficient	In Eq. (3)	4.0	2.0
γ^{C}	MVMM dissipative coefficient	In Eq. (23), $\gamma^{\mathrm{C}} = \gamma^{\mathrm{T}}/3$	30	–
γ^{T}	MVMM dissipative coefficient	In Eq. (23)	90	–
σ^{C}	MVMM random coefficient	In software	–	–
σ^{T}	MVMM random coefficient	In software	–	–
γ	DPD dissipative force coefficient	In Eq. (4)	30	45
σ	DPD random force coefficient	In Eq. (5), by Eq. (6)	2.38	2.76
k_{b}	Bending coefficient	In Eq. (10), by Eq. (22)	5.792558ξ	–
φ_0	Spontaneous angle	In Eq. (10), by Eq. (22)	0°	–

$$\tau = \frac{\eta^{\mathrm{P}}}{\eta^{\mathrm{M}}} \frac{Y^{\mathrm{M}}}{Y^{\mathrm{P}}} \frac{L_0^{\mathrm{P}}}{L_0^{\mathrm{M}}} \tag{30}$$

$$\mu = \frac{Y^P}{Y^M}\tau^2 \tag{31}$$

Based on the analysis, scaling factors in the simulation are summarized in the Table 4.

4.2. Methods of modeling and simulating

The cell-modeling process begins with the use of DistMesh algorithm [52] written by MATLAB to draw triangular mesh based on the input shape in terms of distance function without considering the accurate representation of the number of actins and spectrins [30]. Then, a system-modeling script is constructed using Python to generate simulation model in a data format that can be read by revised version LAMMPS [45,51], which contains the MVMM model.

Periodic boundary conditions are applied in the simulation box. In addition, Lennard-Jones potential functions are added between the droplet particles and cells to serve as bounce-back boundary conditions to prevent emulsion particle transport into the interior of the cell. Walls are also added at the top and bottom of the z-axis to prevent DPD particles from crossing. The particle representing the Pickering emulsion is distributed at the top free-motion zone randomly based on the norm distribution of the average mean velocity and direction vector. An external downward force is applied on the Pickering emulsion to represent the effect of pressure. The cells in the middle of the box are fixed with force to prevent significant displacement due to the effect of the extracellular matrix. At the apical and basal vertices of the cell, additional bonds are introduced to connect with the nearest wall particles, ensuring the stabilization of the cell's position, and reflecting the restrictive role of the extracellular matrix on cell movement.

Table 4
Scaling factor between physical units and model units

Symbol	Meaning	Notice	Value
λ	Length unit (m)	By Eq. (26)	1×10^{-6}
ξ	Energy unit (J)	By Eq. (27)	4.81586×10^{-20}
ϵ	Force unit (N)	By Eq. (28)	4.81586×10^{-14}
ν	Pressure unit (Pa)	By Eq. (29)	4.81586×10^{-2}
τ	Time unit (s)	By Eq. (30)	2.70518×10^{-3}
μ	Mass unit (kg)	Eq. (31)	3.52425×10^{-13}

5. Results

To evaluate the efficiency of the transport phenomenon of Pickering emulsion between muscular cells, the criteria is selected as the diffusion coefficient, which is obtained by the mean square of displacement (MSD) [47] and transport time along the fixed distance from the end to end. In the following, Fig. 3 shows the ensembled averaged MSD result of Pickering emulsion, which demonstrates a near-linear relationship with the time delta.

We initially examined the conservative force parameter *a* in DPD, investigating its values at 1.0, 2.0 and 3.0. It can be observed from the Fig. 4 that as the conservative force parameter *a* increases, the diffusion coefficient of the Pickering emulsion decreases, and the diffusion time correspondingly increases. This outcome illustrates the role of parameter *a* in modulating inter-particle interactions, which in turn affects the diffusion behavior of particles in the emulsion. Given that the conservative force in the DPD method represents the radial repulsive force between a pair of particles, it can indicate that an increase in *a* leads to enhanced repulsive forces between particles, resulting in greater particle separation and a reduced likelihood of particle movement due to concentration gradients. This enhanced repulsion may cause particles to be more dispersed in space, thereby increasing the difficulty and time required for them to diffuse to a specific region. Moreover, the reduction in diffusion coefficient and the increased transport time may also imply a more stable spatial organization of Pickering emulsion particles. In certain applications, such as drug delivery systems, this increased stability may be beneficial as it can slow down the release of active components. However, for processes that require rapid diffusion and mixing, such as in catalytic reactions, increased repulsive forces and decreased diffusion coefficients may not be desirable effects. There is a potential link between particle characteristics (such as surface modification or polarity size) and the DPD conservative force parameter. If emulsion particles are modified on their surface to enhance their interactions, this could lead to an increase in repulsion, thereby affecting the diffusion process. This indicates that the design and optimization of emulsions should consider not only the chemical properties of the particles but also their interactions in the simulation environment.

Furthermore, the impact of local cellular tissue environmental factors on the transport efficiency of Pickering emulsion is investigated, as shown in Figs. 5–7. The driving force applied to the Pickering emulsion can be approximated as the pressure in the local tissue cellular environment or the external driving force from the muscle injection process or the driving force from

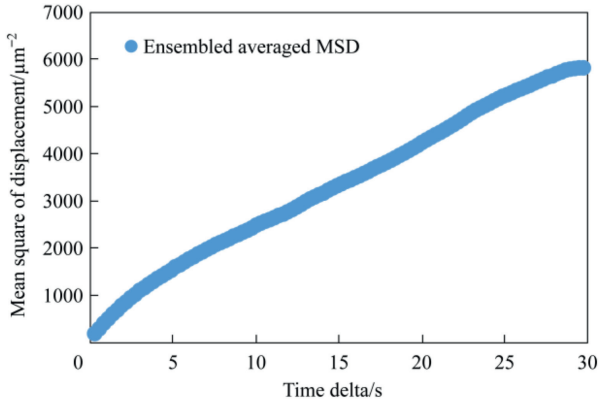

Fig. 3. Ensemble averaged mean square of displacement (MSD).

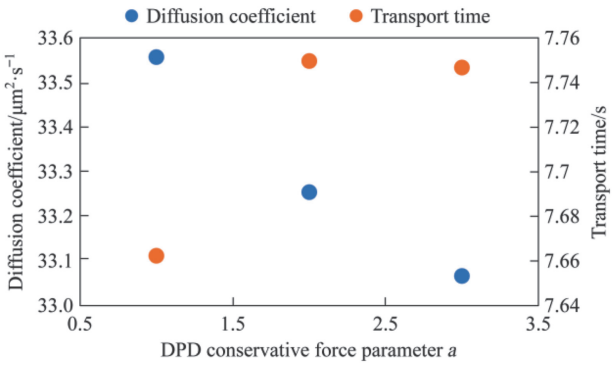

Fig. 4. The influence of DPD conservative force parameter of Pickering emulsion.

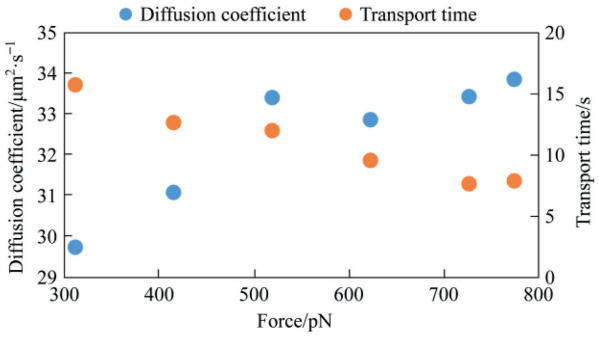

Fig. 5. The influence of pushing force on Pickering emulsion.

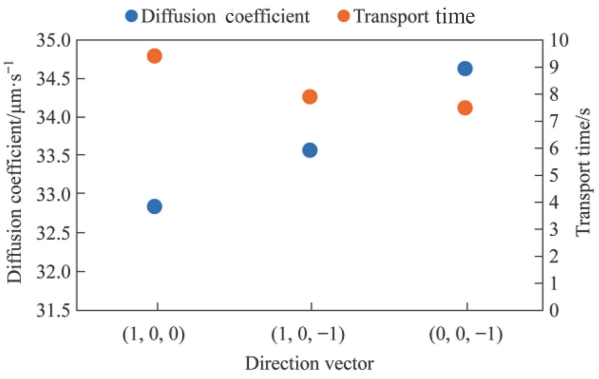

Fig. 6. The influence of the direction vector of Pickering emulsion.

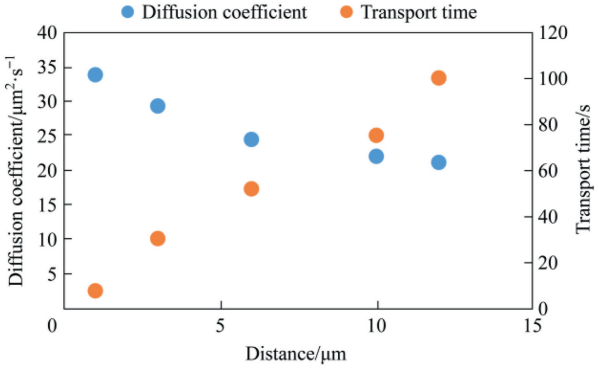

Fig. 7. The influence of size of gaps between cells.

concentration differences. Under these driving forces, Fig. 5 indicates that the Pickering emulsion droplets would traverse through the intercellular gaps within the tissue faster under greater local driving forces. The increased diffusion coefficient with higher applied force suggests that the droplets are experiencing less resistance in the medium, allowing them to spread more quickly. This could be due to the fact that higher forces help to overcome the various frictional and viscous forces that act on the droplets, facilitating their movement through the tissue matrix. Conversely, the decrease in transport time with increased force implies that the droplets can reach their target sites more rapidly. This is particularly relevant in medical applications, where the time-sensitive delivery of therapeutic agents is crucial. The ability to control the transport time of the emulsion droplets by adjusting the applied force could lead to more efficient and targeted drug delivery strategies. By fine-tuning the applied force, it may be possible to enhance the penetration of droplets through the intercellular gaps of tissues, ensuring that the active agents are distributed evenly and that they reach the site of action effectively. Moreover, the relationship between force and transport properties could be further exploited to understand the interaction of droplets with complex tissue structures. For example, in dense or fibrous tissues, higher forces might be required to achieve the same level of diffusion as in less dense tissues. Understanding these relationships can aid in the design of emulsion-based delivery systems that are customized for specific tissue types and therapeutic needs.

Concurrently, the influence of the statistic average initial velocity vector direction of the Pickering emulsion on its transport efficiency was examined. Fig. 6 presents the impact of the initial velocity vector direction of Pickering emulsion droplets on their transport efficiency. The direction vector (1, 0, 0) represents a direction perpendicular to the axial alignment of the cells, whereas the direction vector (0, 0, −1) represents a direction parallel to the axial alignment of the cells. It is observable that the transport efficiency is higher when the average direction vector of the velocity is closer to the axial alignment direction of the cells. Intuitively, when the movement direction of droplets is aligned with the principal axis of the cells, their path through the intercellular gaps is more direct, which may reduce the resistance they encounter during motion, thereby enhancing transport efficiency. These findings emphasize the importance of considering not only the chemical and physical properties of emulsion droplets in the design of emulsion-based drug delivery systems but also their kinematic characteristics, including the direction of the velocity vector. By adjusting the initial direction of velocity during the injection or delivery process, the delivery path and timing of therapeutic agents can be optimized.

Moreover, in the modeling, the size of the intercellular gaps between cells is altered to inspect the influence of the cellular environment within the tissue on the Pickering emulsion. Fig. 7 denotes that larger intercellular gaps lower the diffusion coefficient, while the transport time of the Pickering emulsion consequently increases. The results shown in Fig. 7 might seem counterintuitive to initial assumptions, which could be attributed to the following reasons: Here, the Pickering emulsion droplets have an average initial velocity direction that is perpendicular to the axial alignment of the cells. Therefore, lateral diffusion contributes significantly to the diffusion process, and the increase in intercellular gaps markedly lengthens the path for lateral diffusion. This increases the likelihood of encountering obstacles or taking more circuitous paths, as the droplets are more influenced by interactions with the spaces between cells, with an increased chance of collisions, thereby enhancing the complexity of the path during diffusion. This complexity leads to a significant increase in energy dissipation throughout the diffusion process, thereby reducing the droplets' kinetic energy, resulting in a decreased diffusion coefficient and increased transport time. Typically, studies on near-wall hindered diffusion focus on a single channel, whereas the transport phenomena examined here within the tissue present a complexity that goes far beyond a single channel; specifically, for Pickering emulsion droplets, the contributions resulting from longer lateral diffusion distances, more complex diffusion pathways, and more frequent interactions with the walls of the diffusion channels outweigh the contributions from single near-wall hindered events [53], thus exhibiting the characteristics seen in Fig. 7.

Further investigations are conducted on other factors affecting the transport performance of Pickering emulsion, including viscosity (represented by the DPD dissipative force parameter gamma), temperature, interaction between Pickering emulsion and cell (represented by DPD conservative force parameter between DPD particle and cell model), and the initial velocity magnitude of Pickering emulsion. Considering the fluctuation–dissipation theorem and the fact that the shear modulus of cells changes with variations in environmental temperature, Table 5 summarizes the impact of temperature variations on various parameters within the model. Table 6 summarizes the variance values of the diffusion coefficient under the influence of various parameters, indicating that the variance of the γ_{particle} parameter of DPD emulsion droplets is the smallest, implying that surface viscosity has a relatively smaller impact on the transport of Pickering emulsion than do the other parameters listed here.

Notice that this study did not consider the adhesion influence between cells and emulsion particles, which could further decrease the transport efficiency of Pickering emulsion droplets between tissues and affect the distribution of Pickering emulsion in a real muscular tissue environment. Besides, in order to reflect the pressure within tissue, this simulation is during an unsteady process. The current model only incorporates the effects of radial repulsive conservative forces; Some research work [54–57]

Table 6
Analysis of variance of simulation parameters

Parameter	Range	Mean value	Variance
γ_{particle}	25–45	0.085007429	1.89194×10^{-6}
a_{inter}	1–5	0.088832662	5.66877×10^{-6}
T /K	296–314	0.090481135	8.93948×10^{-6}
Velocity /μm·s^{-1}	4–15	0.092851366	7.54986×10^{-6}

Table 5
Analyses for parameters of temperature

T /K	$(k_BT)^P$/J	$(k_BT)^M$	σ_{Particle}	σ_{cell}	μ_0^P /N·m^{-1}	μ_0^M
296	4.08672×10^{-21}	0.084859	2.7635	2.2564	6.3×10^{-6}	100.00
303	4.18336×10^{-21}	0.086866	2.7960	2.2829	6.16×10^{-6}	97.73
308	4.25239×10^{-21}	0.088299	2.8190	2.3017	6.12×10^{-6}	97.20
310	4.28001×10^{-21}	0.088873	2.8281	2.3091	5.8×10^{-6}	92.06
312	4.30762×10^{-21}	0.089446	2.8372	2.3166	5.39×10^{-6}	85.60
314	4.33523×10^{-21}	0.090020	2.8463	2.3240	4.9×10^{-6}	77.78

considering DPD particles with fixed charge may suggest the potential to include the effects of charge forces in the model.

6. Conclusions

Based on the elaborated results and discussions, the following conclusions can be drawn regarding the transport phenomenon of Pickering emulsion between muscular cells.

(1) The transport efficiency of Pickering emulsion is significantly influenced by a variety of factors including the conservative force parameter in the DPD method, local cellular tissue environmental factors, viscosity, temperature, interaction between Pickering emulsion and cell, and the initial velocity magnitude of Pickering emulsion.
(2) The impact of the local cellular environment within the tissue significantly affects the transport efficiency of Pickering emulsion. Specifically, greater local driving forces, which could be due to the pressure in the local tissue cellular environment or external driving forces from muscle injection process or concentration differences, expedite the traversal of Pickering emulsion droplets through the intercellular gaps within the tissue. Moreover, the orientation of the initial velocity vector of the Pickering emulsion toward the axial direction of the cells enhances the transport efficiency. Conversely, an increase in the size of the intercellular gaps leads to a decrease in the diffusion coefficient and an increase in the transport time of the Pickering emulsion.
(3) An increase in the conservative force parameter a in the DPD method, representing the radial repulsive force between particles, leads to a decrease in the diffusion coefficient and a corresponding increase in diffusion time of the Pickering emulsion. This suggests that a larger mutual repulsive force among Pickering emulsion particles potentially results in lower transport efficiency. The magnitude of this repulsive force could be attributed to factors such as the surface modification or polarity size of the Pickering emulsion. Among other investigated factors, the variance of the gamma parameter of DPD emulsion droplets is found to be the smallest, suggesting that surface viscosity has a relatively lesser impact on the transport of Pickering emulsion.

These findings provide a comprehensive understanding of the various factors affecting the transport efficiency of Pickering emulsion between muscular cells, which is crucial for optimizing the transport process in practical applications. The insights gained from this study could be instrumental in designing more effective transport systems for Pickering emulsion, thereby facilitating its potential applications in drug delivery and other relevant fields.

Additionally, based on the analysis of the physiological structure of lymphatic capillaries and collecting vessels, the 2-micron-wide pillow structures on capillary lymphatics, which open and close under interstitial to intraluminal pressure gradients, may provide a pathway for fluid transport for the transportation of Pickering emulsion. This mechanism potentially facilitates the movement of Pickering emulsion within the lymphatic system, thereby broadening the understanding of how the physiological architecture can influence the transport dynamics of Pickering emulsion. This aspect exemplifies the interdependence between biological structures and the transport phenomena of nano- or micro-scale emulsions such as Pickering emulsion, enriching the comprehension of how engineering and biological systems can be integrated for enhanced performance in biomedical applications.

Declaration of Interest

The authors declare that they have no known competing financial interests or personal relationships that could have appeared to influence the work reported in this manuscript.

Acknowledgements

This study is financially supported by the National Natural Science Foundation of China (22373104 and 22293024) and the Science Fund for Creative Research Groups of the National Natural Science Foundation of China (21821005). This study is also supported by the National Key Research and Development Program of China (2021YFE020527). Yufei Xia is grateful for the support by the Distinguished Young Scholars of the National Natural Science Foundation of China (T2222022). We also acknowledge the computational resources provided by upgraded Mole-8.5E supercomputing system developed by Institute of Process Engineering, Chinese Academy of Sciences.

References

[1] Y.Q. Yang, Z.W. Fang, X. Chen, W.W. Zhang, Y.M. Xie, Y.H. Chen, Z.G. Liu, W.E. Yuan, An overview of Pickering emulsions: solid-particle materials, classification, morphology, and applications, *Front. Pharmacol.* 8 (2017) 287.
[2] Y.F. Xia, J. Wu, W. Wei, Y.Q. Du, T. Wan, X.W. Ma, W.Q. An, A.Y. Guo, C.Y. Miao, H. Yue, S.G. Li, X.T. Cao, Z.G. Su, G.H. Ma, Exploiting the pliability and lateral mobility of Pickering emulsion for enhanced vaccination, *Nat. Mater.* 17 (2018) 187–194.
[3] A. Azuar, H.Y.R. Madge, J.C. Boer, J.L. Gonzalez Cruz, J. Wang, Z.G. Khalil, C. Deceneux, G. Goodchild, J. Yang, P. Koirala, W.M. Hussein, R.J. Capon, M. Plebanski, I. Toth, M. Skwarczynski, Poly(hydrophobic amino acids) and liposomes for delivery of vaccine against group A streptococcus, *Vaccines* 10 (8) (2022) 1212.
[4] J. Liu, X.D. Yan, X.Q. Li, Y.H. Du, L.L. Zhu, T.T. Ye, Z.Y. Cao, Z.W. Dong, S.T. Li, X. Xu, W. Bai, D. Li, J.W. Zhang, S.J. Wang, S.H. Li, J. Sun, X.Z. Yin, Chrysanthemum sporopollenin: A novel vaccine delivery system for nasal mucosal immunity, *Front. Immunol.* 14 (2023) 1132129.
[5] L.S. Ming, H.L. Wu, A. Liu, A. Naeem, Z.S. Dong, Q.M. Fan, G.C. Zhang, H.N. Liu, Z. Li, Evolution and critical roles of particle properties in Pickering emulsion: A review, *J. Mol. Liq.* 388 (2023) 122775.
[6] J. Pielenhofer, J. Sohl, M. Windbergs, P. Langguth, M.P. Radsak, Current progress in particle-based systems for transdermal vaccine delivery, *Front. Immunol.* 11 (2020) 266.
[7] Y.L. Ming, Y.F. Xia, G.H. Ma, Aggregating particles on the O/W interface: Tuning Pickering emulsion for the enhanced drug delivery systems, *Aggregate* 3 (2) (2022) e162.
[8] A. Schudel, D.M. Francis, S.N. Thomas, Material design for lymph node drug delivery, *Nat. Rev. Mater.* 4 (6) (2019) 415–428.
[9] T.T. Song, Y.F. Xia, Y.Q. Du, M.W. Chen, H. Qing, G.H. Ma, Engineering the deformability of albumin-stabilized emulsions for lymph-node vaccine delivery, *Adv. Mater.* 33 (26) (2021) e2100106.
[10] J.J. Chen, Z.F. Ye, C.F. Huang, M. Qiu, D.H. Song, Y.M. Li, Q.B. Xu, Lipid nanoparticle-mediated lymph node-targeting delivery of mRNA cancer vaccine elicits robust $CD8^+$ T cell response, *Proc. Natl. Acad. Sci. USA* 119 (34) (2022) e2207841119.
[11] G.P. Howard, N.G. Bender, P. Khare, B. López-Gutiérrez, V. Nyasembe, W.J. Weiss, J.W. Simecka, T. Hamerly, H.Q. Mao, R.R. Dinglasan, Immunopotentiation by lymph-node targeting of a malaria transmission-blocking nanovaccine, *Front. Immunol.* 12 (2021) 729086.
[12] H. Qin, R.F. Zhao, Y.T. Qin, J. Zhu, L. Chen, C.Z. Di, X.X. Han, K.M. Cheng, Y.L. Zhang, Y. Zhao, J. Shi, G.J. Anderson, Y.L. Zhao, G.J. Nie, Development of a cancer vaccine using *in vivo* click-chemistry-mediated active lymph node accumulation for improved immunotherapy, *Adv. Mater.* 33 (20) (2021) e2006007.
[13] P. Baluk, J. Fuxe, H. Hashizume, T. Romano, E. Lashnits, S. Butz, D. Vestweber, M. Corada, C. Molendini, E. Dejana, D.M. McDonald, Functionally specialized junctions between endothelial cells of lymphatic vessels, *J. Exp. Med.* 204 (10) (2007) 2349–2362.
[14] J.W. Breslin, Mechanical forces and lymphatic transport, *Microvasc. Res.* 96 (2014) 46–54.
[15] A.R. Gillies, R.L. Lieber, Structure and function of the skeletal muscle extracellular matrix, *Muscle Nerve* 44 (3) (2011) 318–331.
[16] S. Jalkanen, M. Salmi, Lymphatic endothelial cells of the lymph node, *Nat. Rev. Immunol.* 20 (9) (2020) 566–578.
[17] K.N. Margaris, R.A. Black, Modelling the lymphatic system: Challenges and opportunities, *J. R. Soc. Interface* 9 (69) (2012) 601–612.

[18] J.P. Nederveen, M.W. Betz, T. Snijders, G. Parise, The importance of muscle capillarization for optimizing satellite cell plasticity, *Exerc. Sport Sci. Rev.* 49 (4) (2021) 284–290.
[19] L.H. Nicoll, A. Hesby, Intramuscular injection: An integrative research review and guideline for evidence-based practice, *Appl. Nurs. Res.* 15 (3) (2002) 149–162.
[20] O. Ohtani, Y. Ohtani, C.J. Carati, B.J. Gannon, Fluid and cellular pathways of rat lymph nodes in relation to lymphatic labyrinths and Aquaporin-1 expression, *Arch. Histol. Cytol.* 66 (3) (2003) 261–272.
[21] F. Zhang, G. Zarkada, S.J. Yi, A. Eichmann, Lymphatic endothelial cell junctions: Molecular regulation in physiology and diseases, *Front. Physiol.* 11 (2020) 509.
[22] E. Mendoza, G.W. Schmid-Schönbein, A model for mechanics of primary lymphatic valves, *J. Biomech. Eng.* 125 (3) (2003) 407–414.
[23] N.P. Reddy, K. Patel, A mathematical model of flow through the terminal lymphatics, *Med. Eng. Phys.* 17 (2) (1995) 134–140.
[24] N.Q. Gong, Y.X. Zhang, Z. Zhang, X.L. Li, X.J. Liang, Functional nanomaterials optimized to circumvent tumor immunological tolerance, *Adv. Funct. Mater.* 29 (3) (2019) 1806087.
[25] D.A. Fedosov, B. Caswell, G.E. Karniadakis, A multiscale red blood cell model with accurate mechanics, rheology, and dynamics, *Biophys. J.* 98 (10) (2010) 2215–2225.
[26] N. Liu, M. Becton, L.Y. Zhang, X.Q. Wang, Mechanism of coupling nanoparticle stiffness with shape for endocytosis: From rodlike penetration to wormlike wriggling, *J. Phys. Chem. B* 124 (49) (2020) 11145–11156.
[27] W. Pan, A.M. Tartakovsky, Dissipative particle dynamics model for colloid transport in porous media, *Adv. Water Resour.* 58 (2013) 41–48.
[28] L. Zhou, S.L. Feng, H.T. Liu, J.Z. Chang, Dissipative particle dynamics simulation of cell entry into a micro-channel, *Eng. Anal. Bound. Elem.* 107 (2019) 47–52.
[29] H.J. Liu, Y. Sun, C.A. Simmons, Determination of local and global elastic moduli of valve interstitial cells cultured on soft substrates, *J. Biomech.* 46 (11) (2013) 1967–1971.
[30] I.V. Pivkin, G.E. Karniadakis, Accurate coarse-grained modeling of red blood cells, *Phys. Rev. Lett.* 101 (11) (2008) 118105.
[31] P.J. Hoogerbrugge, J.M.V.A. Koelman, Simulating microscopic hydrodynamic phenomena with dissipative particle dynamics, *Europhys. Lett.* 19 (3) (1992) 155–160.
[32] J.M.V.A. Koelman, P.J. Hoogerbrugge, Dynamic simulations of hard-sphere suspensions under steady shear, *Europhys. Lett.* 21 (3) (1993) 363–368.
[33] X.J. Fan, N. Phan-Thien, S. Chen, X.H. Wu, T. Yong Ng, Simulating flow of DNA suspension using dissipative particle dynamics, *Phys. Fluids* 18 (6) (2006) 063102.
[34] D.A. Fedosov, G.E. Karniadakis, B. Caswell, Dissipative particle dynamics simulation of depletion layer and polymer migration in micro- and nano-channels for dilute polymer solutions, *J. Chem. Phys.* 128 (14) (2008) 144903.
[35] P. Español, P. Warren, Statistical mechanics of dissipative particle dynamics, *Europhys. Lett.* 30 (4) (1995) 191–196.
[36] P. Español, Fluid particle model, *Phys. Rev. E* 57 (3) (1998) 2930–2948.
[37] W. Pan, D.A. Fedosov, G.E. Karniadakis, B. Caswell, Hydrodynamic interactions for single dissipative-particle-dynamics particles and their clusters and filaments, *Phys. Rev. E Stat. Nonlin. Soft Matter Phys.* 78 (4 Pt 2) (2008) 046706.
[38] W. Pan, I.V. Pivkin, G.E. Karniadakis, Single-particle hydrodynamics in DPD: A new formulation, *Europhys. Lett.* 84 (1) (2008) 10012.
[39] D.E. Discher, D.H. Boal, S.K. Boey, Simulations of the erythrocyte cytoskeleton at large deformation. II. Micropipette aspiration, *Biophys. J.* 75 (3) (1998) 1584–1597.
[40] J. Li, M. Dao, C.T. Lim, S. Suresh, Spectrin-level modeling of the cytoskeleton and optical tweezers stretching of the erythrocyte, *Biophys. J.* 88 (5) (2005) 3707–3719.
[41] D.A. Fedosov, G. Gompper, White blood cell margination in microcirculation, *Soft Matter* 10 (17) (2014) 2961–2970.
[42] A. Yazdani, Y. Deng, H. Li, E. Javadi, Z. Li, S. Jamali, C. Lin, J.D. Humphrey, C.S. Mantzoros, G.E. Karniadakis, Integrating blood cell mechanics, platelet adhesive dynamics and coagulation cascade for modelling thrombus formation in normal and diabetic blood, *J. R. Soc. Interface* 18 (175) (2021) 20200834.
[43] M. Razizadeh, M. Nikfar, R. Paul, Y.L. Liu, Coarse-grained modeling of pore dynamics on the red blood cell membrane under large deformations, *Biophys. J.* 119 (3) (2020) 471–482.
[44] X. Shi, G. Lin, J.F. Zou, D.A. Fedosov, A lattice Boltzmann fictitious domain method for modeling red blood cell deformation and multiple-cell hydrodynamic interactions in flow, *Int. J. Numer. Meth. Fluids* 72 (8) (2013) 895–911.
[45] A.L. Blumers, Y.H. Tang, Z. Li, X.J. Li, G.E. Karniadakis, GPU-accelerated red blood cells simulations with transport dissipative particle dynamics, *Comput. Phys. Commun.* 217 (2017) 171–179.
[46] C. Pozrikidis, Computational Hydrodynamics of Capsules and Biological Cells, CRC Press, Boca Raton, FL, 2010.
[47] M.P. Allen, D.J. Tildesley, Computer Simulation of Liquids, second ed., Oxford University Press, Oxford, United Kingdom, 2017.
[48] M. Dao, J. Li, S. Suresh, Molecularly based analysis of deformation of spectrin network and human erythrocyte, *Mater. Sci. Eng. C* 26 (8) (2006) 1232–1244.
[49] B. Liu, X. Qiu, How to compute the atomic stress objectively? *J. Comput. Theor. Nanos.* 6 (5) (2008) 1082–1089.
[50] L.L. Zhang, J. Jasa, G. Gazonas, A. Jérusalem, M. Negahban, Extracting continuum-like deformation and stress from molecular dynamics simulations, *Comput. Meth. Appl. Mech. Eng.* 283 (2015) 1010–1031.
[51] Y.H. Tang, G.E. Karniadakis, Accelerating dissipative particle dynamics simulations on GPUs: Algorithms, numerics and applications, *Comput. Phys. Commun.* 185 (11) (2014) 2809–2822.
[52] P.O. Persson, G. Strang, A simple mesh generator in MATLAB, *SIAM Rev.* 46 (2) (2004) 329–345.
[53] S. Eloul, E. Kätelhön, R.G. Compton, When does near-wall hindered diffusion influence mass transport towards targets? *Phys. Chem. Chem. Phys.* 18 (38) (2016) 26539–26549.
[54] M. González-Melchor, E. Mayoral, M.E. Velázquez, J. Alejandre, Electrostatic interactions in dissipative particle dynamics using the Ewald sums, *J. Chem. Phys.* 125 (22) (2006) 224107.
[55] R.D. Groot, Electrostatic interactions in dissipative particle dynamics—simulation of polyelectrolytes and anionic surfactants, *J. Chem. Phys.* 118 (24) (2003) 11265–11277.
[56] A. Gubbiotti, M. Chinappi, C.M. Casciola, EH-DPD: A dissipative particle dynamics approach to electrohydrodynamics, *Eur. Phys. J. Plus* 137 (5) (2022) 572.
[57] J. Smiatek, F. Schmid, Mesoscopic simulations of electroosmotic flow and electrophoresis in nanochannels, *Comput. Phys. Commun.* 182 (9) (2011) 1941–1944.